Nanoindentation Hardness and Modulus of Al_2O_3-SiO_2-CaO and MnO-SiO_2–FeO Inclusions in Iron

Author(s):
Slagter, Alejandra; Setyadji, Jonathan Aristya; Vogt, Eva Luisa; Hernández-Escobar, David; Deillon, Léa; Mortensen, Andreas

Publication date:
2024

Permanent link:
https://doi.org/10.3929/ethz-b-000664971

Originally published in:
Metallurgical and Materials Transactions A, https://doi.org/10.1007/s11661-024-07330-x

ORIGINAL RESEARCH ARTICLE

Nanoindentation Hardness and Modulus of Al_2O_3–SiO_2–CaO and MnO–SiO_2–FeO Inclusions in Iron

ALEJANDRA SLAGTER, JONATHAN ARISTYA SETYADJI, EVA LUISA VOGT, DAVID HERNÁNDEZ-ESCOBAR, LÉA DEILLON, and ANDREAS MORTENSEN

Oxide inclusions appear in steel as a subproduct of steelmaking. These are generally detrimental to alloy properties; however, variations exist in the extent to which different inclusions are harmful because their properties vary as a function of their chemical composition. We use nanoindentation to measure the local elastic modulus and hardness of individual oxide particles, produced by precipitation within liquid iron, that belong to the systems Al_2O_3–SiO_2–CaO and MnO–SiO_2–FeO. Measured inclusion hardness values are typically in the range of 8 to 13 GPa and can reach 26 GPa for alumina-rich inclusions. Calcium aluminates rich in alumina are significantly stiffer than iron, with elastic moduli that can reach 350 GPa. On the contrary, calcium aluminates that are expected as a result of successful calcium treatment (*i.e.*, with less than about 80 wt pct Al_2O_3 content) have elastic moduli below that of iron. This is also the case for the wide range of calcium aluminosilicates and of manganese silicates studied here. In addition, silicates containing about 70 to 80 wt pct MnO are observed to have a fine multiphase structure and an elastic modulus of $\approx$ 180 GPa. Those inclusions thus emerge as possible candidates if one aims to minimise, in loaded steel, stress concentrations associated with matrix-inclusion elastic mismatch.

https://doi.org/10.1007/s11661-024-07330-x

I. INTRODUCTION

OXIDE inclusions are micrometre-sized particles that arise in iron-based alloys as necessary sub-products of steel manufacturing processes. Beyond a few specific exceptions where oxide inclusions can be advantageous (*e.g.*, because inclusions can serve as a nucleating agent for acicular ferrite in welded structures[1,2]), their presence in iron-based alloys is often linked to lowered toughness and ductility together with premature fatigue failure.[3–6]

To mitigate the adverse effects associated with the presence of oxide inclusions, efforts in steel production focus on minimising their size and number; however, obtaining steel completely free of inclusions is technologically challenging.[7–10] Recognising that steel processing influences the characteristics of oxide inclusions and that some oxide particles will inevitably be trapped in the steel microstructure, an alternative approach involves adjusting steel processing conditions to produce the least harmful inclusions. This is implemented, for example, in tire cord steel production, where hard alumina inclusions are avoided by processing steel to promote the formation of silicate inclusions that have lower melting points and can better accompany steel deformation during hot forming operations.[11,12] This strategy, however, requires that the characteristics that render inclusions more or less harmful be understood. Inclusion characteristics that are deemed important depend on the steel application; these generally include elastic modulus, hardness, thermal expansion coefficient (CTE), particle strength, and deformability under steel hot-working conditions.[3,6,13–15] This strategy of course also requires that those local inclusion characteristics be known for the various possible inclusion types and chemical compositions.

The chemistry of observed inclusions is primarily determined by steel processing conditions including, in the first place, the type of deoxidant used: commonly used elements are Al, Si and Mn. Another critical factor

ALEJANDRA SLAGTER, EVA LUISA VOGT, DAVID HERNÁNDEZ-ESCOBAR, and ANDREAS MORTENSEN are with the Laboratory of Mechanical Metallurgy, École Polytechnique Fédérale de Lausanne, 1015 Lausanne, Switzerland. Contact e-mail: alejandra.slagter@epfl.ch, andreas.mortensen@epfl.ch JONATHAN ARISTYA SETYADJI is with the Laboratory of Mechanical Metallurgy, École Polytechnique Fédérale de Lausanne and also with the Nanyang Technological University, 50 Nanyang Ave, Singapore 639798, Singapore. LÉA DEILLON is with the Laboratory of Mechanical Metallurgy, École Polytechnique Fédérale de Lausanne and also also with the Department of Mechanical and Process Engineering, ETH Zürich, Technoparkstr. 1, 8005 Zürich, Switzerland.
Manuscript submitted October 12, 2023; accepted January 22, 2024.

Published online: 27 February 2024

is the possible use of additional processing steps to modify existing inclusions. For example, alumina inclusions produced in the course of Al-deoxidation are often *treated* with Ca to form liquid calcium aluminates, thus avoiding solid alumina inclusions, which have a tendency to clog the nozzles that feed continuous casting moulds.[10,16] Other factors that can affect the inclusion composition, though to a smaller extent, are the type of slag and the chemistry of refractories used in steel production.[17]

The end result is that inclusions in steel products are often multi-metal oxides that appear in myriad compositions. Inclusions are often based on oxides of Al, Si, Mn, and Ca, at times with smaller fractions of other elements such as Mg or Ti (see, *e.g.,* Refs. 18 through 20). Despite this variety of possible compositions and ensuing inclusion microstructures, local inclusion properties are well documented only for simple mono-metallic or stoichiometric bi-metal oxides, with scarce data beyond those few oxides. The most extended database of inclusion properties is that of Kiessling and Lange,[13] which compiles, along with physical properties such as the melting point and density, microhardness data for stoichiometric compounds in the $Fe_xMn_{1-x}O$–SiO_2–$Cr_yAl_{2-y}O_3$, MgO–SiO_2–Al_2O_3, and CaO–SiO_2–Al_2O_3 systems. Data on the deformability of a more limited range of inclusion compositions are also available in Reference 13 while thermal expansion coefficients of some types of oxide inclusions have been compiled by Brooksbank and Andrews.[21,22]

Concerning the elastic modulus, data for stable oxides that have other technological interest or that appear naturally on the Earth's crust, such as SiO_2, various silicates, Al_2O_3, and some aluminates, are available, for example, in References 23 through 25. In addition, a few reports exist that measure this property directly on oxide inclusions using nanoindentation, a technique capable of probing volumes of material as small as a few cubic micrometres and therefore compatible with the micrometre size of typical inclusions observed in steel.[26,27] Pioneering work in this respect was performed by Lamagnere *et al.*[28] and with added contributions by Stiénon *et al.*[29] and Wagner *et al.*[30] Other reports of the use of nanoindentation to measure inclusion properties include the work of Kushe *et al.*[31] and of Wang *et al.*,[32] though the former is not concerned with oxide inclusions (but rather manganese sulphides) and the latter only reports hardness values and not elastic modulus. Other than for stable oxides of technological interest, information on the elastic properties of several inclusions that are commonly found in steel, such as calcium aluminates, is scarce: to the best of our knowledge, available data are limited to indentation measurements on only two out of six possible single-phase calcium aluminates visible on the CaO–Al_2O_3 pseudo-binary diagram,[28,29] and to values produced by first-principles simulations.[33,34] This is surprising given that calcium aluminates have been reported to be among the most harmful type of oxide inclusions in steel alloys subjected to fatigue[35,36] while also the inclusion elastic modulus is recognised as a key parameter governing the stress distribution around inclusions and hence plays, together with the inclusion size, inclusion–matrix interface strength, inclusion shape and thermal expansion coefficient, an important role in internal damage processes such as fatigue crack nucleation and propagation in steels.[36–41] Given that, despite the increased cleanliness of modern steel,[42] complete elimination of the oxide inclusion population is not likely to be possible for mass-produced steel, a better knowledge of the mechanical properties of oxides that form in steel should provide a useful design tool, allowing for further improvements in steel performance.

We present here a study in which we produce a wide range of oxide inclusion compositions within laboratory-scale samples of iron, to then measure their elastic modulus and hardness by nanoindentation. We explore in this manner the influence of composition across two relatively wide ranges in the Al_2O_3–SiO_2–CaO system (including various types of calcium aluminates) and also in a more limited region of the MnO–SiO_2–FeO system.

II. MATERIALS AND METHODS

Samples were produced by deoxidation experiments in which a few grams of pure iron (99.98 pct purity, *abcr* GmbH, Karlsruhe, Germany) are co-melted with small additions of deoxidising agents in the form of silicon, manganese, aluminium and/or $CaSi_2$. The chemical composition of the iron lumps as provided by the supplier (and not comprising the oxygen content) is presented in Table I. The iron lumps additionally contained trace amounts of oxygen, in the range of 200 to 300 ppm as measured using the inert gas fusion technique, along with some surface oxide. Oxygen from these two sources combined with the deoxidant additions to form small quantities of oxide inclusions by precipitation within the liquid iron. Details of the amounts and types of deoxidising agents are presented in Table II.

The melting operation was carried out in an argon atmosphere either by induction melting (in a silica crucible or in a cold crucible setup as described in Reference 43) or by arc-melting. These different techniques were used along process flows detailed in Figure 1 to explore the effect of processing parameters on the characteristics of obtained inclusions. In the end, differences were minor and mainly observed on the spatial distribution of inclusion within the iron sample and not among the characteristics of the individual particles. The composition of resulting inclusions was a function of the deoxidant nature and concentration (itself strongly altered by calcium loss by evaporation in samples containing this element) and on location within the sample.

Samples were prepared for metallographic characterisation using standard metallographic procedures. Because many of the calcium aluminate oxide particles gave indications of being etched by water, all grinding and polishing operations for samples containing those inclusions were performed using ethanol as the lubricant, while a mixture of water, soap, and ethanol was used for other samples. Polished surfaces were observed

Table I. Chemical Composition of High-Purity Iron Lumps Used as Indicated in the Certificate of Analysis (*abcr* GmbH, Karlsruhe, Germany)

Iron Lumps Composition [Wt Pct]						
Fe	C	Mn	Ni	P	S	Si
99.98	0.0008	0.0002	0.0022	0.00022	0.0015	0.0002

using a Zeiss Gemini 300 (Oberkochen, Germany) scanning electron microscope (SEM) under a voltage of 3 kV. The same instrument, equipped with an energy-dispersive X-ray spectroscopy (EDS) detector (Oxford Instruments, Abingdon, UK) was used to determine the elemental inclusion compositions *after* nanoindentation testing of the particles so as to: (i) avoid potential electron beam-induced artefacts that may arise on the surface of the oxide from prolonged EDS acquisition times (typically > 30 s) and (ii)

Table II. Deoxidising Agents, Crucible, and Melting Technique Used to Produce Iron Samples Containing Oxide Inclusions

Sample	Crucible/Furnace for Final Melting	Deoxidising Agent	Wt Pct Al Added	Wt Pct $CaSi_2$ Added	Wt Pct Si Added	Wt Pct Mn Added
1	Fused quartz (SiO_2)/induction	$CaSi_2$*	0	0.12	—	—
2	Refrigerated copper/arc	Al, $CaSi_2$*	1.07	0.88	—	—
3	Refrigerated copper/induction	Al, $CaSi_2$*	1.05	0.90	—	—
4	Refrigerated copper/induction	Al, $CaSi_2$*	1.08	1.13	—	—
5	Refrigerated copper/arc	Al, $CaSi_2$*	1.03	0.90	—	—
6	Refrigerated copper/induction	Si, Mn	—	—	0.62	4.53
7	Refrigerated copper/induction	Si, Mn	—	—	0.31	1.17

*$CaSi_2$ used in this study was in powder form (*Sigma-Aldrich*) and was found *via* EDS measurements to contain variable concentrations, situated on average around 1.8 wt pct of Al as an impurity.

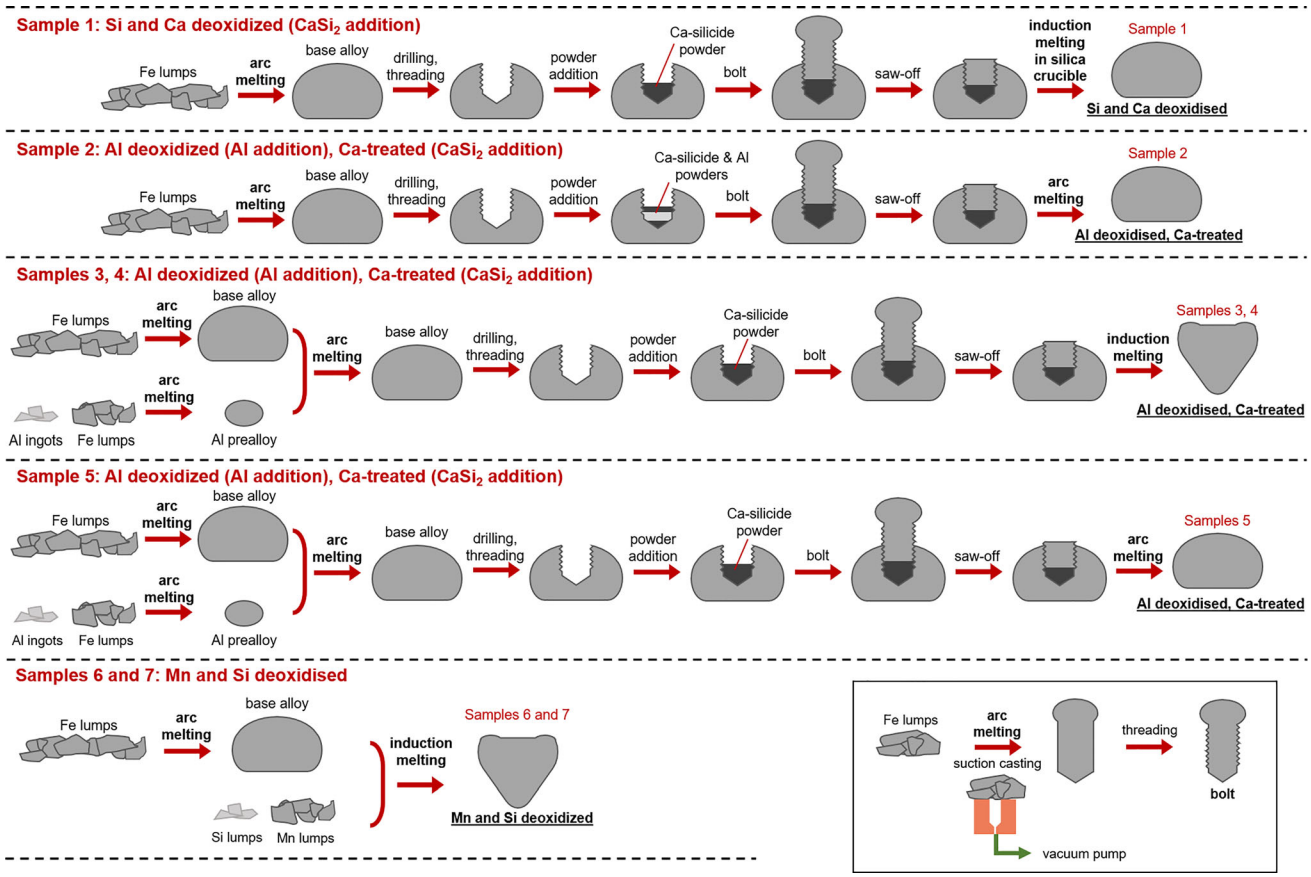

Fig. 1—Detailed fabrication processing route of the seven samples characterised in this work. Different routes were implemented to produce inclusions with various compositions. Iron bolts were made by the vacuum arc melting technique with vacuum casting into a cylindrical mould, followed by machining, and were used to keep the added powder enclosed within the iron sample up to melting. Deoxidation in Sample 1 and Ca-treatment in Samples 2 to 5 were made using $CaSi_2$ (Color figure online).

precisely analyse the composition of the indented region, in particular in multiphase inclusions. The operating voltage for EDS measurements was between 6 and 15 kV. Cation ratios were used to determine single cation oxide fractions assuming oxygen stoichiometries corresponding to FeO, MnO, CaO, Al_2O_3, and SiO_2.

Thermodynamic calculations aiming to predict inclusion compositions were performed with the Thermo-Calc^{TM} software using the TCOX9 database. A first series of calculations was carried out considering the nominal composition of Sample 1 (deoxidised only with $CaSi_2$) with the goal of explaining the range of observed compositions (see Results). The silicon content was set to 0.07 wt pct of the total sample mass, coexisting in the molten iron along with different amounts of Ca, which were set as a percentage of nominal additions to simulate various scenarios of Ca evaporation during sample preparation. The oxygen content used for the calculations was 200 ppm, this being the approximate value measured by the inert gas fusion technique in the pure iron lumps used here. The presence of aluminium was also examined since this element is present as an impurity in the $CaSi_2$ that was used as a deoxidant in sample preparation. More specifically, the content of Al detected by EDS in the $CaSi_2$ powder varied significantly (from 0.6 to 23 wt pct Al after deconvoluting the carbon content) when measured at various locations along an ≈ 11 mm^2 area of carbon tape covered with the powder. It was on average 1.8 wt pct of the $CaSi_2$, and in calculations the aluminium content was thus varied from 5 to 75 ppm by mass within the molten iron sample.

The computations were performed suspending from the database all crystalline phases associated with silica. This was motivated by (i) the spherical shape of present high-silica inclusions (which suggests that they are not crystalline), and (ii) the fact that amorphous phases have been reported for a wide area of the ternary Al_2O_3–SiO_2–CaO oxides.[44] The phases suspended from the database were thus cristobalite, tridymite, quartz and mullite. The simulations were run for a temperature of 1600 °C and a pressure of 10^5 Pa, and hence correspond to (metastable) thermodynamic equilibrium microstructures predicted at that temperature, which we assume are roughly maintained given the rapid subsequent cooling of the samples.

Nanoindentation was carried out using a Hysitron TI 950 (Bruker, Billerica, MA) equipped with a Berkovich diamond tip, and was performed along the sample cross-section after it was polished with diamond paste down to 0.25 μm. Individual inclusions were labelled before nanoindentation by writing a number, using focused ion beam (FIB) milling, into the neighbouring iron matrix tens of micrometres away from the inclusion (Figure 2(a)) to subsequently allow a direct correlation between the individual inclusion composition and its resulting modulus and hardness. The scanning probe microscopy (SPM) capability of the nanoindenter was used to produce a topographical image of each inclusion before and after indentation, which enabled precise localization of the indents on the oxide particles with a spatial resolution of 500 nm, Figures 2(b) through (d). The loading sequence included a linear loading segment, a hold at maximum load, and a linear unloading segment. Maximum loads were in the range of 900 μN to 1300 μN. For most of the inclusions, one indentation was made per particle in a location as close as possible to the centre of the particle; for the few cases where more than one nanoindentation measurement was made per oxide particle, reported values correspond only to the first indent.

III. RESULTS

A. *Inclusion Chemical Composition*

In each iron sample investigated, inclusion compositions were observed to vary, with no apparent correlation between composition and location within the sample, across a relatively wide range of chemistries; measured compositions are superimposed in the liquidus projection of the respective ternary systems in Figures 3(a) and (b). To better understand these observations, thermodynamic simulations were carried out using the Thermo-Calc^{TM} software with the TCOX9 database taking as an example the nominal composition of Sample 1 (deoxidised only with $CaSi_2$). Results of these simulations are presented in Figures 3(c) and (d). The dark symbol in Figure 3(c) (100 pct Ca yield) shows the predicted inclusion composition obtained by assuming that the entire deoxidiser addition of $CaSi_2$ plus 10 ppm Al (corresponding to about 1 wt pct of the $CaSi_2$ addition) is incorporated and dissolved into iron containing 200 ppm O. In the calculations, the influence of small amounts of Si that might have been incorporated to the melt (by reaction with the SiO_2 crucible used to

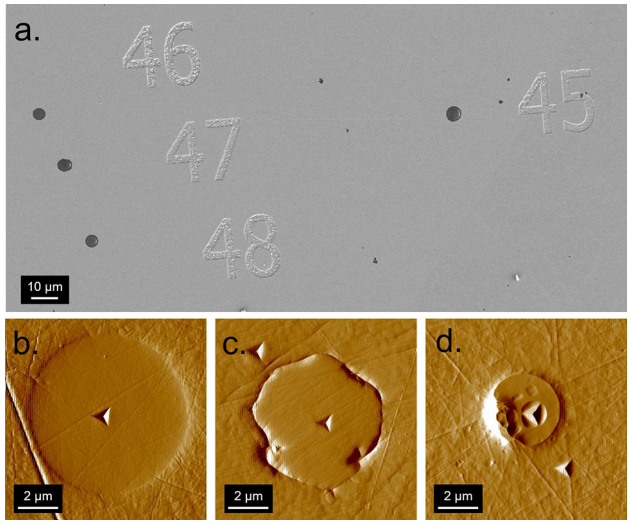

Fig. 2—(*a*) SE-SEM micrograph of four spherical oxide inclusions and their labels, written into the iron matrix using focused ion beam milling; (*b*) through and (*d*) gradient scanning probe microscopy (SPM) images of selected inclusions in the Al_2O_3–CaO system obtained after nanoindentation testing, with (d) showing pileup around the indentation site (light/dark areas correspond to variations in the force sensed by the tip while scanning and not directly to topography).

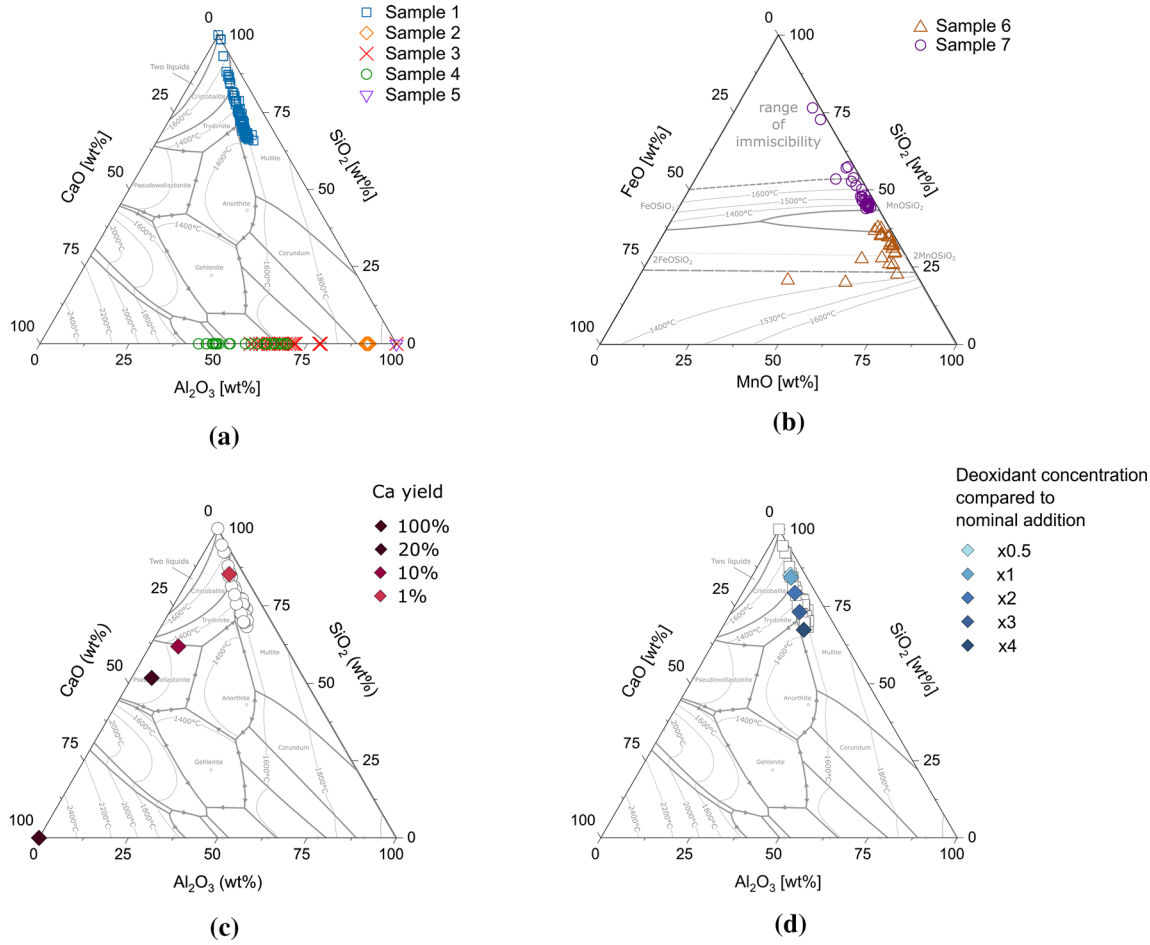

Fig. 3—(*a, b*) chemical composition (determined by EDS) of individual oxide inclusions tested by nanoindentation (a) in the system Al_2O_3–SiO_2–CaO and (b) in the system MnO–SiO_2–FeO; (*c, d*) results of thermodynamic predictions for the nominal composition of Sample 1 considering (c) different extents of Ca evaporation (100 pct Ca yield corresponding to no evaporation and 1 pct Ca yield corresponds to 99 pct of Ca being evaporated), and (d) different scenarios of deoxidant concentration, with x1 deoxidant concentration corresponding to the experimental addition of Si, a Ca yield of 1 pct, and 10 ppm Al (other deoxidant concentrations correspond to lower or higher dilutions into iron but keeping the same proportions of deoxidant elements and 200 ppm O). In (c, d), except for the point corresponding to 100 pct CaO where the predicted phase corresponds to ''halite'', all other inclusions compositions were predicted as liquid oxides. Ternary liquidus projections for a, c&d) are redrawn from Ref. [45] liquidus projections for (b) are redrawn from Ref. [46] (Color figure online).

melt Sample 1) were not considered, given that iron with 200 ppm of dissolved oxygen would be in equilibrium with SiO_2 if the amount of Si dissolved in iron was on the order of 250 ppm: this amount is negligible in comparison with that of Si added from $CaSi_2$ (about 0.07 wt pct). The predicted inclusion composition then corresponds to pure CaO.

If one bears in mind that calcium does not dissolve in iron and that the boiling point of calcium is below the melting point of iron, and if therefore one assumes that a certain fraction of the calcium is lost by evaporation (while other elements remain), then one obtains the other points in that figure for various scenarios of calcium yield, Figure 3(c). As seen, with 1 pct of the calcium retained the predicted inclusion chemistry falls along the line of measured compositions. If then one thus assumes that 99 pct of the calcium evaporates from the $CaSi_2$ deoxidant addition when it is added to the molten iron, and now varies the ratio of deoxidiser elements (with only 1 pct of the initial calcium content entering the melt) to deoxidised alloy (iron plus 200 ppm oxygen), then predicted oxide equilibrium compositions, as shown in Figure 3(d), lie along the same line as those observed experimentally for Sample 1.

In the simulations, various other combinations of Ca evaporation level, Al impurity level in the $CaSi_2$, and initial oxygen concentration were found to lead to similar results (those are presented in the Supplementary Materials). While the absolute concentrations assumed here for Ca, Al, and O may therefore not accurately match those of the tested samples, the order of magnitude is likely to be correct, and variations explored here in their relative ratios thus offer a plausible explanation for observed inclusion chemical compositions.

B. *Inclusion Morphology and Structure*

The typical aspect of inclusions, as observed in SEM images of metallographic cross sections, is presented in Figure 4. Inclusions appeared often as isolated

micrometre-sized particles; however, alumina inclusions were generally found as aggregates (Figure 4(e)) and rarely appeared as isolated inclusions (Figure 4(d)). Many of the produced inclusions were nearly spherical: such was the case for all inclusions in Samples 1, 6 and 7, and for many of the inclusions in Samples 2 to 5. Some inclusions presented irregular facets; this was notably the case for inclusions with composition close to $CaO{\cdot}6Al_2O_3$, Figure 4(c).

As observed in Figures 4(f) and (i), complex inclusions consisting of multiple oxide phases were also observed. This was the case for nearly all manganese-silicate inclusions in Sample 7 where a matrix with composition close to $MnO{\cdot}SiO_2$ was observed to contain precipitates of composition close to SiO_2, Figure 4(i). On the MnO-SiO_2 phase diagram, one finds that above roughly 45 wt pct SiO_2, solidification of SiO_2 precedes that of $MnO{\cdot}SiO_2$, consistent with the observed two-phase oxide structures observed here in inclusions of Sample 7. Similar multiphase inclusion structures were also observed for some calcium aluminates, where a matrix of composition in the neighbourhood of $CaO{\cdot}Al_2O_3$ (but with the Al/Ca ratio varying across the range from 1.4 to 3.0) was often observed to contain inclusions of composition near $CaO{\cdot}6Al_2O_3$, Figure 4(f). Occasionally, and most frequently in calcium-rich oxide particles, sulphur-containing precipitates were found next to, or within, the oxide particles (Figure 4(a)). This last observation is in line with the literature, which documents the co-precipitation of sulphide and oxide inclusions, as well as an affinity of sulphur for calcium (see, *e.g.*, Fig. 8 of Reference 47 or Fig. 5 of Reference 37). Sulphur in the present samples has its origin as an impurity in the iron lumps (Table I).

C. *Nanoindentation Response*

Nanoindentation data obtained from oxide inclusions that displayed, in optical or high voltage scanning electron microscopy, a uniform microstructure along the plane of polish are plotted in Figure 5. Results obtained by indentation testing on inclusions that appeared to contain several phases, found in Sample 7 (with structures as in Figure 4(i)) and Samples 2 to 5 (with structures as in Figure 4(f)), being more uncertain due to the influence of neighbouring secondary phases within the same inclusion, are only presented in the Supplementary Materials.

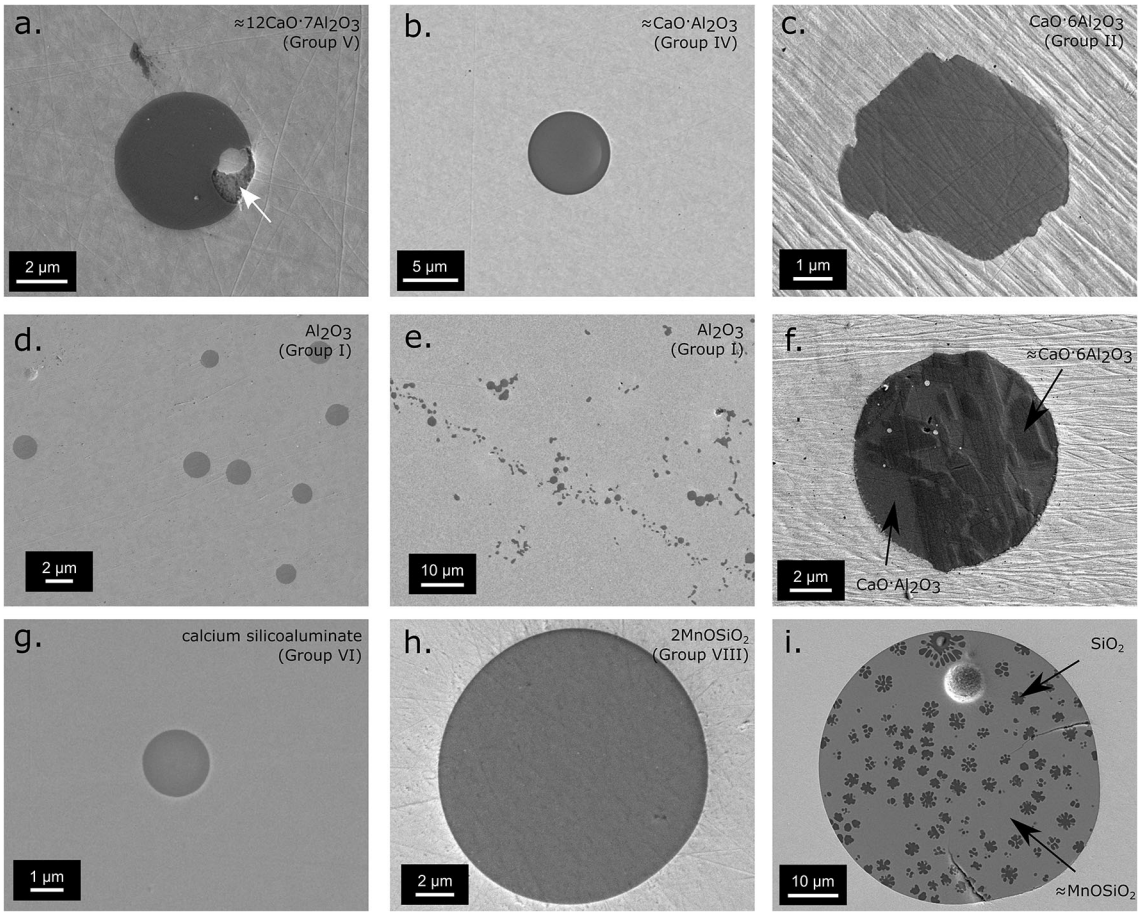

Fig. 4—Scanning electron microscopy images of some representative oxide inclusions observed in samples of this work. Images (*a*) to (*f*) show inclusions in the $CaO–Al_2O_3$ system while images (*g*) to (*i*) show silica-based inclusions. In (a) the white arrow points at a sulphur rich phase (a situation most often seen in Ca-rich oxides). Group numbers refer to composition ranges shown in Fig. 5 and described in Sect. IV.

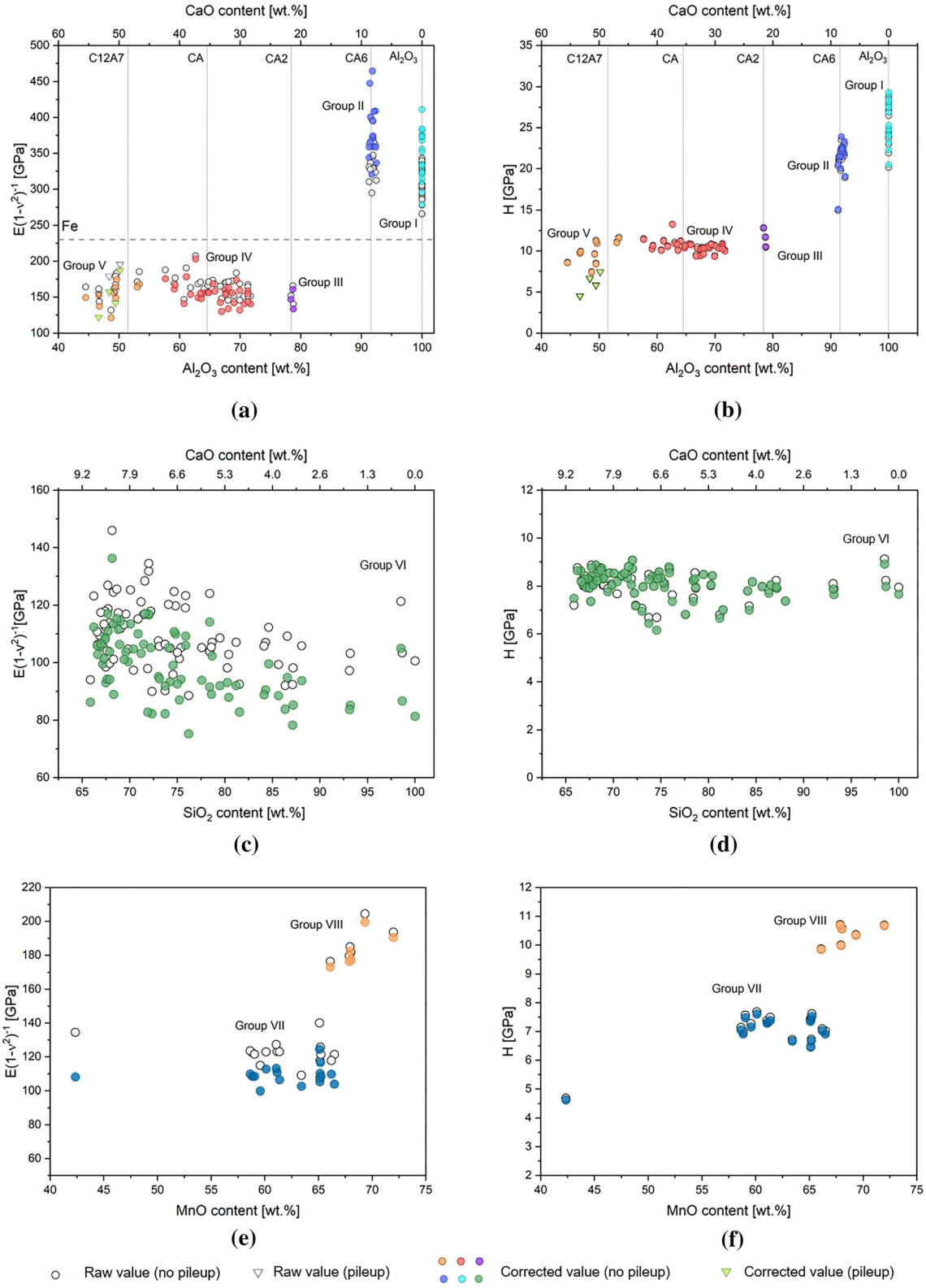

Fig. 5—Elastic modulus and hardness of calcium aluminates (*a, b*), calcium aluminosilicates (*c, d*), and manganese silicates (*e, f*). Each data point corresponds to the indentation of a single inclusion; white-filled symbols are obtained by directly applying the Oliver–Pharr method[26,27] to the indentation data collected; colour-filled symbols are additionally corrected for the average matrix elasticity contribution following the method described in Ref. [55] Inverted triangles in (a) and (b) indicate indentations in which signs of pileup were observed in SPM images after indentation; presented data has not been corrected for pileup but only for matrix elasticity contributions. Composition is reported here as the wt pct of Al_2O_3 (a, b), SiO_2 (c, d), MnO (e, f), or CaO (top horizontal scale) in the inclusion composition. The locations of the corresponding composition ranges for each sample are illustrated on the ternary diagrams in Fig. 3 (Color figure online).

Because the load measured during nanoindentation is sensitive not only to the material immediately below the indenter but also to long-range stress fields, elastic modulus measurements on small volumes of materials can be affected by the properties of the surrounding matrix or substrate.[32,48–55] In Figure 5, data obtained by direct application of the Oliver–Pharr method[26,27] (i.e., ignoring the multiphase nature of the tested material and thus assuming that the material below the indenter is homogeneous) are presented as white-filled symbols. Colour-filled symbols correspond to the same indentation data after correction for matrix elasticity contributions using the method described in Reference 55 in which the particles are assumed to behave as spheres partially embedded in an homogeneous material of different elastic properties. More specifically, the matrix elasticity correction has been applied using an average correction factor alpha value of 1.06 (as suggested in Reference 55 for spherical particles) and taking the matrix properties to be those of steel, namely an elastic modulus of 210 GPa and a Poisson ratio of 0.3. Results are presented using the value returned by nanoindentation, namely $E/(1-\nu^2)$, rather than Young's modulus (E) of the inclusion, to avoid assuming a value for the inclusion Poisson ratio (ν).

IV. DISCUSSION

A. *Inclusion Composition*

By comparing the chemistry of inclusions identified in Sample 1 with the results derived from thermodynamic computations described above it is possible to provide a plausible scenario explaining why compositions in that sample vary and lie along the observed line (Figure 3(d)). If the precipitation of oxide inclusions takes place before melt homogenisation, then variations in observed inclusion chemical compositions will be induced by variations in the local concentration of deoxidiser, which is in turn a result of incomplete mixing. Furthermore, if solute transport is mostly by convection, as is reasonable for short times, then the relative ratio (but not the concentration) of dissolved deoxidising element concentrations will be the same everywhere (note that we also assume here that Ca evaporation from, and the Al impurities in, the $CaSi_2$ additions are both uniform across the small amount of powder used for deoxidation of Sample 1). As seen in Figure 3(d), if one assumes that only 1 pct of the Ca in the $CaSi_2$ is incorporated while other elements remain, and if furthermore the local concentration of these deoxidising elements varies within the Fe-200 ppm O melt while Ca/Si and Al/Si ratios remain constant, then one obtains a series of inclusion concentrations that lie neatly along the line of measured inclusion chemistries. This shows that local variations in the concentration of dissolved deoxidiser agents at the time of oxide formation can explain the observed range of inclusion chemistries in Sample 1 (Figure 3(a)) if these are governed by local equilibrium at 1600 °C and remain unchanged over time and during solidification.[17]

Unlike Sample 1, which was prepared by adding a single deoxidising agent ($CaSi_2$), Samples 2 to 7 were prepared by adding multiple deoxidising agents (Table I). Local deoxidiser concentration variations in these samples then do not only lead to variations in the ratio of deoxidiser to deoxidised alloy (iron plus oxygen), but also to various ratios between the different deoxidant elements. This is likely the reason why a larger spread of inclusion compositions is observed in other samples, and why compositions for Sample 6, shown in the ternary diagram of Figure 3(b), cover an area rather than a line or a curve. In Samples 2 to 5, inclusion compositions do not depart from the line

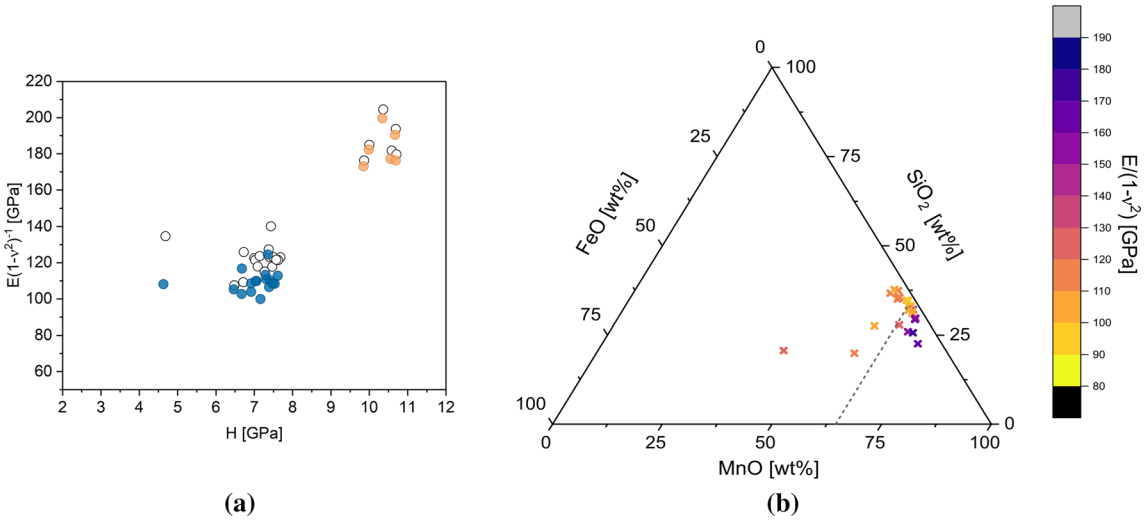

Fig. 6—Elastic modulus and hardness results obtained for inclusions in Groups VII and VIII showing (*a*) that data are clustered into two groups and (*b*) that the clusters in property values are correlated with the MnO content. White-filled symbols in (a) represent raw indentation data while coloured-filled symbols represent data corrected for the average matrix elasticity contribution following the method described in Ref. [55] (Color figure online).

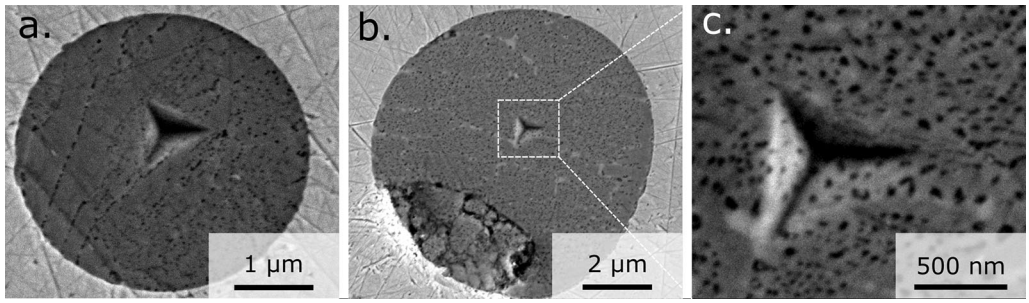

Fig. 7—Scanning electron microscopy images (SE detector) with examples of fine multiphase structure observed on inclusions in Groups VII (image *a*) and VIII (images *b* and *c*).

joining CaO and Al_2O_3; this is not surprising given the far stronger oxygen affinity of Al and Ca compared to other oxide-forming elements present in the melt (Si and Fe), coupled with the much higher concentration of the former elements as compared with those in Sample 1, thus causing Si additions to remain dissolved in the iron.

B. *Inclusion Structure*

Inclusions in Groups I, II, and III (Figure 5(a) and (b)) correspond to phases for which the EDS data fall in narrow compositional ranges and have stoichiometries corresponding to Al_2O_3 (Group I), $CaO{\cdot}6Al_2O_3$ (Group II, referred to hereafter as CA6; see Figure 5 for definitions of short-hand oxide compositions) and $CaO{\cdot}2Al_2O_3$ (Group III, or CA2), respectively. Electron backscatter diffraction (EBSD) analysis was carried out on inclusions from each of these three groups (data are given in the Supplementary Materials). This confirms, through the presence of Kikuchi lines, the crystalline nature of Group I, II and III inclusions, as suggested by their relatively stoichiometric chemical compositions.

Inclusions in Groups IV and V (Figures 5(a) and (b)) present wider compositional ranges. These bear no relation to the $CaO–Al_2O_3$ pseudo-binary phase diagram, as there are no wide single-phase fields predicted for solid phases in that region of the phase diagram. Moreover, EBSD analysis conducted on inclusions from these groups do not exhibit Kikuchi lines. Given these observations and the consistently spherical inclusion morphology in those two groups, it is highly likely that inclusions in Groups IV and V are amorphous. Our classification of these inclusions into two groups, namely Group IV or V, is thus based exclusively on their chemistry falling within a certain range, with the boundary between the two Groups placed at 55 wt pct Al_2O_3. This line of separation was chosen instead of the stoichiometric composition of the phase, namely 12 $CaO{\cdot}7Al_2O_3$, because this is where the largest gap runs between the two sets of datapoints. We note in passing that inclusions in Group V are ones where sulphur-containing phases were identified, either within, or adjacent to, the oxide inclusions (Figures 2(d) and 4(a)).

Inclusions in Group VI (Figures 5(c) and (d)) contain more than two-thirds of silica by weight. They display a consistently spherical morphology and have compositions known to produce, in macroscopic samples, oxide glasses when air-cooled from 1600 °C.[44] Inclusions in Group VI are therefore likely amorphous. Due to the large range of compositions of inclusions in this group and to the observed trend of modulus decrease with increasing silica content (Figure 5(c)), indentation data for inclusions in this group were binned by composition, with a bin every 5 wt pct SiO_2, before averaging to account for the matrix influence on nanoindentation data.

Inclusions in Group VII and VIII correspond to manganese silicate oxides. These appear to be single-phased upon observation at low magnification or with high voltage in the SEM. Results of indentation testing of these inclusions, however, are clearly clustered into two groups, suggesting that two different types of inclusions were in fact present, Figure 6(a). As observed in Figure 6(b), the transition in properties correlates roughly with the MnO content and (surprisingly) not with the total MnO + FeO content, as would be expected if the transition in properties was caused by the overall inclusion composition crossing the $2Mn_xFe_{1-x}SiO_4$ boundary (which runs as a horizontal line at about 30 wt pct SiO_2 in the ternary diagrams of Figures 3b and 6b). Upon SEM imaging with higher resolution and with the use of carbon coating to decrease charging effects, some inclusions in Groups VII and VIII exhibited a multiphase microstructure, Figure 7. The presence of this multiphase structure was somewhat more frequent in inclusions of Group VIII than in those of Group VII, but a direct correlation was not observed. Upon EBSD analysis, some of the inclusions also show signs of being crystalline, most of them corresponding to inclusions that are also observed to have a multiphase structure, but again with no direct correlation with the Group number. Details of the microstructures and EBSD results are presented in the Supplementary Materials. Finally, small amounts of S detected in inclusions of Groups VII and VIII, in the range of 0.23 to 1.3 at. pct, also show no correlation with hardness and elastic modulus results. The classification of inclusions in each of these groups was therefore made considering only indentation results and not microstructural aspects. Because the microstructural features observed in Figure 7 are considerably smaller than the indentation size (Figure 7(c)), hardness and

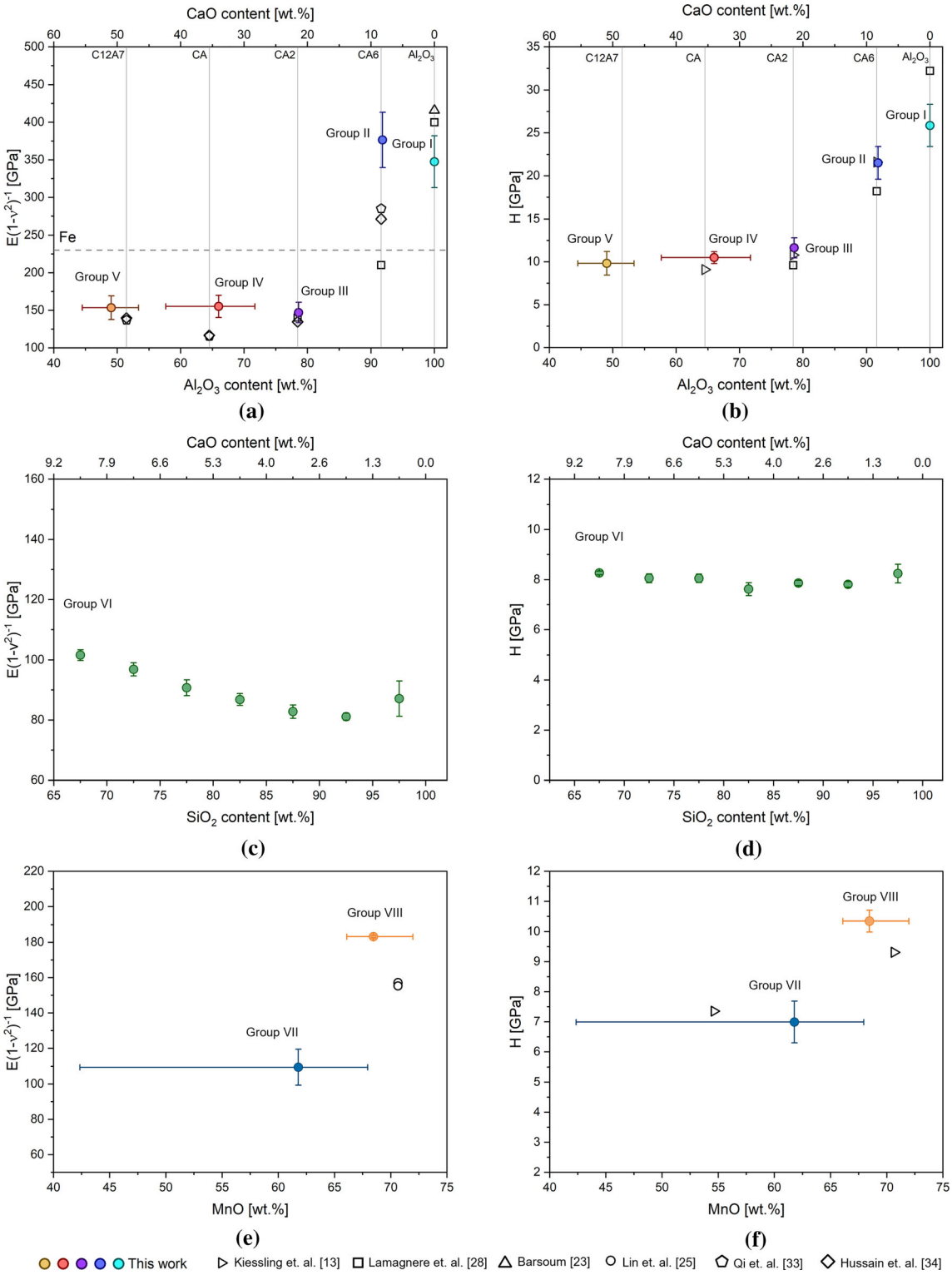

Fig. 8—Average elastic modulus and hardness *vs* average oxide composition for calcium aluminates (*a*, *b*), calcium aluminosilicates (*c*, *d*), and manganese silicates (*e*, *f*); vertical error bars correspond to the standard deviation while horizontal error bars delimit observed compositional ranges). White-filled symbols correspond to literature data for relevant crystalline, stoichiometric oxides[23,25,28,33,34]; in computing $E\ (1 - \nu^2)^{-1}$ from reported E values, Poisson ratios of 0.32 and 0.27 have been assumed for CA2 and CA6 respectively, following Ref. [34] while a value of 0.25 was assumed for Al_2O_3 following Ref. [23] (Color figure online).

elastic modulus values given below are considered to be meaningful, and representative of the multiphase structure.

Overall, most of the inclusions produced and characterised here are apparently single-phased and often amorphous. This might be partly due to the high

Table III. Average Elastic Modulus ($E\,(1-\nu^2)^{-1}$) and Hardness (H) for each Inclusion Group in the $CaO–Al_2O_3$ System, Together with Literature Data for the Density of Stoichiometric Oxides of the Same or Similar Composition

Inclusion Type	Al_2O_3 [Wt Pct] (Mean/Min–Max.)	$(E\,(1-\nu^2)^{-1})$ [GPa] (Mean ± Std. Dev./Min–Max)	H [GPa] (Mean ± Std. Dev./Min–Max)	Density of the Stoichiometric Compound [g·cm^{-3}]
Group I (Al_2O_3)	100	347 ± 35	26 ± 2.5	3.98[57]
Group II ($CaO{\cdot}6Al_2O_3$)	91.8	377 ± 37	22 ± 1.9	3.79[58]
Group III ($CaO{\cdot}2Al_2O_3$)	78.6	147 ± 14	12 ± 1.2	2.92[59]
Group IV (~$CaO{\cdot}Al_2O_3$)	57.6 to 71.7	156 ± 15	10.5 ± 0.7	2.94[60]
Group V (~$12CaO{\cdot}7Al_2O_3$)	44.5 to 53.4	151 ± 19	8 ± 2.0	2.67[61]

Table IV. Average Elastic Modulus ($E\,(1-\nu^2)^{-1}$) and Hardness (H) for Calcium Aluminosilicates and Manganese Silicates

Inclusion Type	SiO_2 [Wt Pct] (min–max.)	$(E\,(1-\nu^2)^{-1})$ [GPa] (Mean ± Std. Dev./Min–Max)	H [GPa] (Mean ± Std. Dev./Min–Max)
Group VI (Ca-aluminosilicates)	65.8 to 100	81 to 102	7.6 to 8.2
Group VII	42.4 to 67.9	109 ± 10	7.0 ± 0.7
Group VIII	66.1 to 72.0	183 ± 0.7	10.3 ± 0.4

cooling-rates that are imposed by the methods used here for sample production; fast cooling might produce homogeneous inclusions with amorphous structures, which would otherwise (if processed more slowly and hence closer to equilibrium) lead to the formation of two or more crystalline phases. We also note that the two types of inclusions for which multiple phases were evident by (relatively) low-magnification imaging in the SEM (and also in SPM images obtained with the nanoindenter in one of the cases) do not correspond to equilibrium microstructures: the matrix and precipitate phases shown in Figure 4(f) are not adjacent in the $CaO–Al_2O_3$ phase diagram, while neither the matrix nor the precipitate shown in Figure 4(i) give any indication of being crystalline in EBSD analysis. In addition, for both multiphase inclusion types, the relatively broad range of chemical compositions observed for the oxide matrix suggests that this part of the inclusion is amorphous.

C. *Local Inclusion Properties: Sources of Uncertainty*

Indentation results presented in Figure 5 show that variations in the inclusion composition can indeed lead to variations in their mechanical properties; however, the dispersion in the obtained results is relatively large both before and after correcting for matrix elasticity contributions. As described in Reference 55 such dispersion in the obtained values is to be expected because inclusions are embedded within iron to different and unknown relative depths, leading the matrix to affect each particle measurement to a different extent. Given that the plane of polish and particle distribution are random, the influence of these variations in particle depth, together with that of uncertainties inherent to the indentation technique, can be reduced by averaging data over a sufficiently large number of inclusions (30 particles or more was found to be sufficient in Reference 55). Since the averaging can only be performed among values from inclusions of the same type, the tested inclusions are classified into eight groups, as described above.

Indentation results, corrected for matrix elasticity contributions and averaged across each of the described inclusion groups are presented in Figure 8 and Tables III and IV. For Groups IV & V, and VII & VIII, the ends of horizontal error bars in Figure 8 indicate the maximum and minimum value of the measured Al_2O_3 or MnO content, respectively. These average results exclude a few indentations in Group V (marked in Figure 5 using triangles as opposed to circles) that exhibited pileup in the topographic SPM images (Figure 1(d)). Such observations of pileup were exclusive to inclusions in that group and did not show any clear correlation with either the inclusion size or chemical composition. No correlation was either found between pile-up and the presence of sulphur-rich phases detected in inclusions belonging to this group.

To account for the uncertainty in present measurements, we consider the two main sources of error mentioned above: (i) uncertainty intrinsic to nanoindentation (related to surface roughness, uncertainty in the zero-load contact point, *etc.*) and (ii) uncertainty associated with the fact that measurements are conducted on particles surrounded by a matrix of different elastic modulus into which the particles are embedded to varying depths. To estimate the latter source of uncertainty associated with the procedure in Reference 55 we take, as extreme deviations, the particles to be embedded in the matrix to an average depth (relative to their diameter) of 30 or 70 pct, as opposed to the assumed 50 pct value that comes with a random depth distribution.

Those two alternative depths correspond to values of parameter alpha of Reference 55 equal to 1.21 and 0.67, respectively, as opposed to the value 1.06 to be used in the averaging procedure of Reference 55. This induces changes in the final result that are generally around 5 pct and do not exceed 11 pct, which are deviations in the range of uncertainty intrinsic to nanoindentation measurements (Table X4.6 of Reference 56). Given that the standard deviation of data in present measurements is on the order of 10 pct, we conclude that the two sources of uncertainty in present measurements are commensurate, and that their cumulative effect is well reflected in the standard deviation that comes with the averaging of binned data points; this is plotted as error bars in Figure 8.

D. *Local Inclusion Properties: Influence of Composition*

1. *Calcium aluminates*

The results presented in Figures 8(a) and (b) and in Table III show that calcium-rich inclusions of Al_2O_3 content ranging from 40 80 wt pct, and therefore covering nearly the entire range of calcium aluminates expected after successful calcium treatment, have properties that are essentially independent of composition, with an elastic modulus well below that of iron regardless of whether the inclusions are apparently amorphous (Groups IV and V) or crystalline (Group III). At higher alumina contents, however, a sharp transition in the properties is observed between inclusions in Groups III and II (corresponding to $CaO{\cdot}2Al_2O_3$ and $CaO{\cdot}6Al_2O_3$, respectively). This transition correlates well with that reported in the literature for the density of those oxides (Table III). An increased bond density is thus a likely factor causing the measured sharp increase in elastic modulus and hardness of Ca–Al–O inclusions.

As seen in Figure 8(b), hardness data collected here for calcium aluminates are in good agreement with values reported for phases or inclusions of similar compositions, notably with previously reported microhardness[13] and nanoindentation data.[28] By contrast, elastic modulus values presented in Figure 8(a) show a higher degree of discrepancy with data in the literature. For Groups V and IV, this difference is not overly significant if one considers that literature values are calculated (from first-principles density functional theory for crystalline phases of similar composition) and not measured.[33,34] For $CaO{\cdot}6Al_2O_3$ inclusions the discrepancy is unexpectedly high: results presented here are well above values from calculations,[33,34] and are far higher than previously reported experimental data obtained by nanoindentation of inclusions in an industrial bearing steel.[28] The fact that the correction for matrix elasticity contributions of Reference 55 was not applied in Reference 28 is not an explanation since the reported elastic modulus is lower than that of steel, nor is elastic anisotropy an explanation since $(C_{11}–C_{12})/2C_{44}$ computed using tensor coefficients reported in References 33 and 34 gives values close to unity. Differences related to the indentation technique *per se* (*e.g.,* to the calibration of the tip area function) are also unlikely since hardness values reported here and in Reference 28 agree (Figure 8(b)). Perhaps alloying additions present in the commercial steels that were tested in Reference 28 played a role, bringing the elastic modulus of Group II inclusions ($CaO{\cdot}6Al_2O_3$) near that of Group III of this work; however, this proposal is purely speculative and would require verification.

2. *Calcium aluminosilicates*

Variations in elastic modulus and hardness of inclusions in Group VI (calcium aluminosilicate) are modest, Figures 8(c) and (d) and Table IV. There is a slight increase in elastic modulus with decreasing silica content starting at 95 wt pct SiO_2: this is in keeping with the literature as the substitution, in an amorphous SiO_2 network, of Si cations with di- or trivalent oxides normally causes an increase in elastic modulus.[62] Elastic properties measured in this work are also in good agreement with those reported for aluminosilicate glasses in Reference 63. The inclusion elastic modulus evolution found here is thus consistent with the literature and shows a slight, yet finite, influence of composition along the composition ranges delineated in Figure 8(c). Group VI hardness values are higher than those reported in Reference 63. This difference might be a consequence of the higher Al_2O_3/CaO ratio (in at. pct) of inclusions in this work (ranging from 1.2 to 2) as compared to data in Reference 63 (≤ 1). The observed variation is reasonable since a higher Al_2O_3/CaO ratio in aluminosilicate glasses is expected to increase the coordination level of aluminum species,[63] increasing the network connectivity and with it the hardness.

3. *Manganese silicates*

For (manganese silicate) inclusions in Groups VII and VIII, a sharp transition in elastic modulus and hardness is observed when the MnO content in the inclusions exceeds $\approx$ 66 wt pct, Figures 8(e) and (f) and Table IV. The elastic modulus value of 183 GPa observed for inclusions in Group VIII is interesting since it comes closer than do all other data of this work to the 231 GPa value characteristic of iron (calculated taking $E = 211.4$ GPa and $\nu = 0.293$[64]). This value of 183 GPa is slightly higher than the $\approx$ 160 GPa that would be expected if inclusions in this Group had the exact composition of $2MnO{\cdot}SiO_2$ and were crystalline[25], Figure 8(e).

Looking more closely at the microstructure of inclusions in Group VIII, one notices that they contain at least two phases: a matrix and a dispersion of small, nanometric, dark inclusions, which are thus of lower atomic number than the matrix in which they are contained. A low grey level in Figure 7, if not caused by variations in the topography, can therefore only be associated with a low average atomic number and thus, in the present system, to a SiO_2-rich second phase. Backscattered electron (BSE) coefficients, which should be proportional to the flux of BSE electrons emitted and therefore to the non-topographical component of the grey level, are estimated to be 0.375 for MnO, 0.312 for $MnOSiO_2$, and 0.334 for $2MnOSiO_2$ (thus being close for those three phases) while the BSE coefficient of SiO_2

is approximately 0.237.[65] The matrix is thus likely of MnO or of MnO-enriched manganese silicate.

Looking then at literature data for the elastic properties of oxides in the MnO-SiO_2 system, one finds that the elastic modulus of manganosite (MnO) has been reported to be on the order of 317 GPa.[66] Furthermore, MnO inclusions precipitated in iron (and thus containing a finite proportion of iron cations given the low deoxidising power of Mn), produced and tested with the same procedure as described above but using only Mn as deoxidising agent, returned a value of 257 ± 16 GPa (with a hardness of 5.6 ± 0.4 GPa; further details and data are presented in the Supplementary Materials). Measured nanoindentation properties for silico manganese inclusions, in conjunction with the observed microstructures, can thus be rationalised if, for inclusions with more than 66 wt pct MnO, phase separation causes the precipitation of a finely dispersed SiO_2-rich phase leaving behind a MnO-enriched matrix, possibly containing precipitated manganosite, which would explain the rise in elastic modulus.

Note that, in equilibrium conditions, the precipitation of a silica-rich phase is not expected for the average chemical composition of inclusions in Group VIII: the explanation proposed here is thus speculative and might be specific to the present rapidly cooled samples. If however this explanation is correct, given that the elastic modulus of manganosite exceeds that of iron, and given that moving to higher silica contents reduces the oxide modulus, it is possible that there be an intermediate composition at which the average two-phase inclusion elastic modulus in the Mn-Si-O system can be made to match that of iron. This would eliminate, in the fully elastic deformation regime, stress concentrations in steel around those particular oxide inclusions.

E. *Local Inclusion Properties: Implications for Steelmaking*

If the present nanoindentation results are now placed in the context of steelmaking, it can be concluded that elastic moduli of oxide inclusions can take values that are either considerably above or below the elastic modulus of steel, while their hardness is generally above that of the steel matrix. This implies that little improvement can be achieved by tailoring inclusion compositions in processes or applications where the room temperature deformability of the inclusions matters (for example to avoid defect formation during cold rolling), while there might be a window of opportunity to improve the performance of steel products where the steel-inclusion elastic mismatch is important, as in high-cycle fatigue. For example, recent finite element simulations by Allison and Pandkar[40] suggest that the rolling contact fatigue resistance can be improved by a decrease in the modulus of inclusions when those values remain above the modulus of the steel and the inclusions are strongly bonded to the matrix. This conclusion is also found to hold in the presence of extending cracks, pores (equivalent to inclusions with $E = 0$) being less detrimental than inclusions stiffer than the steel.[41] Unfortunately, in References 40, 41 as in other studies (*e.g.*, References 67, 68), the case of an inclusion with a finite elastic modulus lower than that of iron was not considered, incidentally showing that, with the exception of MnS, inclusions are generally considered stiffer than iron when in fact they can also be more compliant.

More specifically, while the elastic modulus of calcium aluminosilicates measured here does not change significantly and remains in the range of 87 to 106 GPa, a sharp transition is observed with composition for the elastic modulus of manganese silicates and calcium aluminates. For calcium aluminates, the transition in properties reported here shows that calcium aluminates expected as a result of successful calcium treatment (with Al_2O_3 contents below 80 wt pct) are more compliant than iron, while only Al_2O_3 and $CaO{\cdot}6Al_2O_3$ exceed its elastic modulus significantly. Furthermore, as noted above, in order to minimise stress concentrations caused by elasticity mismatch between inclusions and the matrix, results of this work suggest that manganese silicates with about 70 to 80 wt pct MnO might offer a solution.

We note in closing that this work evidently covers only a fraction of possible inclusion compositions. It is our aim to pursue it further, as there might be inclusion compositions of greater compatibility with steel than was found in present samples. To give one example, drawing from elasticity data for minerals often found on the Earth's mantle or crust, some silicates emerge as interesting alternatives with both an elastic modulus close to that of iron ($E(1-\nu^2)^{-1} = 231$ GPa) and the potential to be a product of efficient deoxidation; these minerals are forsterite (Mg_2SiO_4) and mullite ($3Al_2O_3{\cdot}2SiO_2$), which have reported values of $E(1-\nu^2)^{-1}$ of 214 GPa[69] and 247 GPa,[24] respectively.

V. CONCLUSIONS

Several oxide inclusions across the Al_2O_3–SiO_2–CaO and MnO–SiO_2–FeO systems can be formed by reactive precipitation within oxygen-containing iron, using procedures based on arc- and/or induction-melting. Inclusions thus produced within each given iron sample are observed to have a wide range of chemical compositions, probably as a result of their relative rapid formation in relation to deoxidant homogenisation times. For samples deoxidised with $CaSi_2$, as much as 99 pct of the calcium addition is lost by evaporation, judging by a comparison of thermodynamic simulations with experimentally determined inclusions compositions. Resulting inclusions are single- or multiphase particles, and the phases they contain are frequently (albeit not always) amorphous, perhaps as a result of the rapid cooling characteristic of the present sample production method.

Inclusions thus produced are amenable to testing by means of nanoindentation for their hardness and modulus. Hardness values for tested inclusions remain always above 4 GPa and thus generally exceed values for steel. Measured oxide inclusion elastic moduli include values both below and above those expected

for iron, as they span a range that goes from 81 to 377 GPa. Of particular notice are the following results:

i. Among compositions explored here, Al_2O_3 inclusions and $CaO{\cdot}6Al_2O_3$ inclusions show the highest elastic modulus values, reaching 377 and 347 GPa, respectively. Hardness values for these inclusions are also comparatively high, with averages at 25.9 GPa (Al_2O_3) and 21.5 GPa ($CaO{\cdot}6Al_2O_3$).
ii. Calcium aluminate inclusions with less than about 80 wt pct Al_2O_3 have average elastic moduli on the order of 150 GPa. Therefore, calcium aluminates produced by successful calcium treatment of Al-deoxidised steel are expected to be less stiff than the iron-based matrix. Average hardness values for these calcium aluminates are in the range of 8.3 to 11.6 GPa.
iii. Calcium aluminosilicate inclusions tested here have elastic modulus and hardness values that are relatively unaffected by their chemical composition. These are in the range of 81 to 102 GPa, thus again lower than iron or steel, and 7.6 to 8.2 GPa, respectively.
iv. Manganese silicate inclusions studied here have elastic modulus values that are below that of iron; however, if the MnO content is on the order of 70 to 80 wt pct, multiphase inclusions with a fine microstructure and an elastic modulus of about 183 GPa are obtained. These have, among all the observed inclusions, the smallest elastic mismatch with the iron-based matrix.

ACKNOWLEDGMENTS

This work was sponsored by the Swiss National Science Foundation, Grant No. 200021_182557. JAS acknowledges the support of the CN Yang Scholarship Programme.

FUNDING

Open access funding provided by EPFL Lausanne.

DATA AVAILABILITY

The raw and processed data from this work are available for download from the Zenodo website at https://zenodo.org/ under the following digital object identifier (DOI): https://doi.org/10.5281/zenodo.8421017.

CONFLICT OF INTEREST

The authors declare that they have no conflict of interest.

OPEN ACCESS

SUPPLEMENTARY INFORMATION

The online version contains supplementary material available at https://doi.org/10.1007/s11661-024-07330-x.

REFERENCES

1. A.R. Mills, G. Thewlis, and J.A. Whiteman: *Mater. Sci. Technol.*, 1987, vol. 3, pp. 1051–61. https://doi.org/10.1179/mst.1987.3.12.1051.
2. S.S. Babu: *Curr. Opin. Solid State Mater. Sci.*, 2004, vol. 8, pp. 267–78. https://doi.org/10.1016/j.cossms.2004.10.001.
3. A.L.V. da Costa e Silva: *J. Mater. Res. Technol.*, 2019, vol. 8, pp. 2408–22. https://doi.org/10.1016/j.jmrt.2019.01.009.
4. P.A. Thornton: *J. Mater. Sci.*, 1971, vol. 6, pp. 347–56.
5. R. Lagneborg: in *Swedish Symposium on Non-Metallic Inclusions in Steel*, H. Nordberg and R. Sandström, eds., Uddeholms AB, Hagfors, 1981, pp. 285–352.
6. W. Leslie: *Mech. Work. Steel Process.*, 1982, vol. XX, pp. 3–50.
7. R. Kiessling: *Met. Sci.*, 1980, vol. 14, pp. 161–72.
8. L.E.K. Holappa and A.S. Helle: *J. Mater. Process. Technol.*, 1995, vol. 53, pp. 177–86. https://doi.org/10.1016/0924-0136(95)01974-J.
9. L. Holappa: *Treatise on Process Metallurgy*, Elsevier, Amsterdam, 2014.
10. L. Holappa and O. Wijk: *Treatise on Process Metallurgy*, Elsevier, Amsterdam, 2014.
11. L. Zhang: *Steel Res. Int.*, 2006, vol. 77, pp. 158–69. https://doi.org/10.1002/srin.200606370.
12. L. Zhang, C. Guo, W. Yang, Y. Ren, and H. Ling: *Metall. Mater. Trans. B*, 2018, vol. 49B, pp. 803–11. https://doi.org/10.1007/s11663-017-1134-2.
13. R. Kiessling and N. Lange: *Non-metallic Inclusions in Steel*, 2nd ed., The Metals Society, London, 1978.
14. Y. Murakami: *Metal Fatigue: Effect of Small Defects and Non-metallic Inclusions*, 2nd ed., Academic Press, New York, 2019.
15. A. Gittins: *Int. Met. Rev.*, 1977, vol. 22, pp. 213–21. https://doi.org/10.1179/imtr.1977.22.1.213.
16. S. Kumar, K.K. Keshari, A. Deva, R.K. Singh, S. Roy, V. Kumar, S. Toppo, K. Abhishek, N. Pradhan, and J. Fail: *Anal. Prev.*, 2022. https://doi.org/10.1007/s11668-022-01569-5.
17. B.A. Webler and P.C. Pistorius: *Metall. Mater. Trans. B*, 2020. https://doi.org/10.1007/s11663-020-01949-y.
18. J. Björklund, M. Andersson, and P. Jönsson: *Ironmak. Steelmak.*, 2007, vol. 34, pp. 312–24. https://doi.org/10.1179/174328107X168039.
19. Z. Deng and M. Zhu: *ISIJ Int.*, 2013, vol. 53, pp. 450–58. https://doi.org/10.2355/isijinternational.53.450.

20. P. Kaushik, J. Lehmann, and M. Nadif: *Metall. Mater. Trans. B*, 2012, vol. 43B, pp. 710–25. https://doi.org/10.1007/s11663-012-9646-2.
21. D. Brooksbank and K.W. Andrews: *J. Iron Steel Inst.*, 1972, vol. 210, p. 246.
22. D. Brooksbank and K. Andrews: *J. Iron Steel Inst.*, 1968, vol. 206, p. 595.
23. M.W. Barsoum: *Fundamentals of Ceramics*, McGraw Hill, New York, 1997.
24. H. Ledbetter, S. Kim, D. Balzar, S. Crudele, and W. Kriven: *J. Am. Ceram. Soc.*, 2005, vol. 81, pp. 1025–28. https://doi.org/10.1111/j.1151-2916.1998.tb02441.x.
25. C.-C. Lin and C.-C. Chen: *EJM*, 2011, vol. 23, pp. 35–43. https://doi.org/10.1127/0935-1221/2011/0023-2077.
26. W.C. Oliver and G.M. Pharr: *J. Mater. Res.*, 1992, vol. 7, pp. 1564–83. https://doi.org/10.1557/JMR.1992.1564.
27. W.C. Oliver and G.M. Pharr: *J. Mater. Res.*, 2004, vol. 19, p. 18.
28. P. Lamagnere, D. Girodin, P. Meynaud, F. Vergne, and A. Vincent: *Mater. Sci. Eng. A*, 1996, vol. 215, pp. 134–42. https://doi.org/10.1016/0921-5093(96)10268-9.
29. A. Stiénon, A. Fazekas, J.-Y. Buffière, A. Vincent, P. Daguier, and F. Merchi: *Mater. Sci. Eng., A*, 2009, vol. 513–514, pp. 376–83. https://doi.org/10.1016/j.msea.2009.02.008.
30. R. Wagner, R. Lehnert, E. Storti, L. Ditscherlein, C. Schröder, S. Dudczig, U.A. Peuker, O. Volkova, C.G. Aneziris, H. Biermann, and A. Weidner: *Mater. Charact.*, 2022, vol. 193, 112257. https://doi.org/10.1016/j.matchar.2022.112257.
31. C.F. Kusche, J.S.K.-L. Gibson, M.A. Wollenweber, and S. Korte-Kerzel: *Mater. Des.*, 2020, vol. 193, 108801. https://doi.org/10.1016/j.matdes.2020.108801.
32. Y.-N. Wang, J. Yang, and Y.-P. Bao: *Metall. Mater. Trans. A*, 2015, vol. 46A, pp. 281–92. https://doi.org/10.1007/s11661-014-2596-3.
33. C. Qi, D. Spagnoli, and A. Fourie: *Constr. Build. Mater.*, 2020, vol. 264, 120259. https://doi.org/10.1016/j.conbuildmat.2020.120259.
34. A. Hussain, S. Mehmood, M.N. Rasool, S. Aryal, P. Rulis, and W.Y. Ching: *Indian J. Phys.*, 2016, vol. 90, pp. 917–29. https://doi.org/10.1007/s12648-015-0830-5.
35. Y. Murakami: *Metal Fatigue: Effect of Small Defects and Nonmetallic Inclusions*, 2nd ed. Elsevier, Amsterdam, 2019, pp. 129–62.
36. J. Monnot, B. Heritier, ande J. Cogne: in *Effect of Steel Manufacturing Processes on the Quality of Bearing Steels*, J. Hoo, ed., ASTM International, West Conshohocken, 1988, p. 149. https://doi.org/10.1520/STP26232S.
37. R. Tricot, J. Monnot, and M. Lluansi: *Met. Eng. Q.*, 1972, vol. 12, p. 39.
38. P. Wang, B. Wang, Y. Liu, P. Zhang, Y.K. Luan, D.Z. Li, and Z.F. Zhang: *Scripta Mater.*, 2022, vol. 206, 114232. https://doi.org/10.1016/j.scriptamat.2021.114232.
39. K. Hashimoto, T. Fujimatsu, N. Tsunekage, K. Hiraoka, K. Kida, and E.C. Santos: *Mater. Des.*, 2011, vol. 32, pp. 1605–11. https://doi.org/10.1016/j.matdes.2010.08.052.
40. B. Allison and A. Pandkar: *Int. J. Fatigue*, 2018, vol. 117, pp. 396–406. https://doi.org/10.1016/j.ijfatigue.2018.08.004.
41. A. Melander: *Int. J. Fatigue*, 1997, vol. 19, pp. 13–24. https://doi.org/10.1016/S0142-1123(96)00045-X.
42. C. Gu, M. Wang, Y. Bao, F. Wang, and J. Lian: *Metals*, 2019, vol. 9, p. 476. https://doi.org/10.3390/met9040476.
43. A. Slagter, J. Everaerts, L. Deillon, and A. Mortensen: *Acta Mater.*, 2023, vol. 242, 118437. https://doi.org/10.1016/j.actamat.2022.118437.
44. J.E. Shelby: *J. Am. Ceram. Soc.*, 1985, vol. 68, pp. 155–58. https://doi.org/10.1111/j.1151-2916.1985.tb09656.x.
45. E. Levin, C.R. Robbins, and H.F. McMurdie: *Phase Diagrams for Ceramists*, 2nd ed. American Ceramic Society, Columbus, 1969.
46. M. Allibert, H. Gaye, D. Geiseler, D. Janke, B.J. Keene, D. Kirner, M. Kowalski, J. Lehmann, K.C. Mills, D. Neuschütz, R. Parra, C. Saint-Jours, P.J. Spencer, M. Susa, M. Tmar, and E. Woerman: *Slag Atlas*, 2nd ed. Verein Deutscher Eisenhüttenleute Verlag Stahleisen, Düsseldorf, 1995.
47. S.K. Choudhary and A. Ghosh: *ISIJ Int.*, 2008, vol. 48, pp. 1552–59. https://doi.org/10.2355/isijinternational.48.1552.
48. R. Saha and W.D. Nix: *Mater. Sci. Eng. A*, 2001, vol. 319–321, pp. 898–901. https://doi.org/10.1016/S0921-5093(01)01076-0.
49. R. Saha and W.D. Nix: *Acta Mater.*, 2002, vol. 50, pp. 23–38. https://doi.org/10.1016/S1359-6454(01)00328-7.
50. J. Hay and B. Crawford: *J. Mater. Res.*, 2011, vol. 26, p. 12.
51. J.W. Leggoe: *J. Mater. Res.*, 2004, vol. 19, pp. 2437–47. https://doi.org/10.1557/JMR.2004.0300.
52. W. Yan, C.L. Pun, and G.P. Simon: *Compos. Sci. Technol.*, 2012, vol. 72, pp. 1147–52. https://doi.org/10.1016/j.compscitech.2012.03.019.
53. W. Yan, C.L. Pun, Z. Wu, and G.P. Simon: *Compos. B Eng.*, 2011, vol. 42, pp. 2093–97. https://doi.org/10.1016/j.compositesb.2011.05.002.
54. T.E. Buchheit and T.J. Vogler: *Mech. Mater.*, 2010, vol. 42, pp. 599–614. https://doi.org/10.1016/j.mechmat.2010.02.007.
55. A. Slagter, J. Everaerts, and A. Mortensen: *J. Mater. Res.*, 2023, vol. 38, pp. 1694–1705. https://doi.org/10.1557/s43578-023-00920-2.
56. E28 Committee: *ASTM E2546-15 Practice for Instrumented Indentation Testing*, ASTM International, Conshohocken, 2015. https://doi.org/10.1520/E2546-15.
57. P. Villars: Al_2O_3 Crystal Structure (n.d.). https://materials.springer.com/isp/crystallographic/docs/sd_0541335.
58. P. Villars: $CaO{\cdot}6Al_2O_3$ (CaAl12O19 rt) Crystal Structure (n.d.). https://materials.springer.com/isp/crystallographic/docs/sd_1407801.
59. P. Villars: $CaO{\cdot}2Al_2O_3$ ($CaAl_4O_7$) Crystal Structure (n.d.). https://materials.springer.com/isp/crystallographic/docs/sd_1501502.
60. P. Villars: $CaAl_2O_4$ Crystal Structure (n.d.). https://materials.springer.com/isp/crystallographic/docs/sd_1820193.
61. P. Villars: $12CaO{\cdot}7Al_2O_3$ ($Ca_6Al_7O_{16.5}$) Crystal Structure (n.d.). https://materials.springer.com/isp/crystallographic/docs/sd_1124586.
62. N.P. Bansal, R.H. Doremus, *Handbook of Glass Properties*, Academic Press, New York, 1986. https://doi.org/10.1016/C2009-0-21785-5.
63. A. Pönitzsch, M. Nofz, L. Wondraczek, and J. Deubener: *J. Non-Cryst. Solids*, 2016, vol. 434, pp. 1–12. https://doi.org/10.1016/j.jnoncrysol.2015.12.002.
64. W.F. Gale and T.C. Totemeier, eds.: *Smithells Metals Reference Book*, 8th ed., Butterworth-Heinemann, Oxford, 2004, pp. 1–45. https://doi.org/10.1016/B978-075067509-3/50018-X.
65. J.I. Goldstein, D.E. Newbury, J.R. Michael, N.W.M. Ritchie, J.H.J. Scott, and D.C. Joy: *Scanning Electron Microscopy and X-Ray Microanalysis*, Springer, New York, 2018. https://doi.org/10.1007/978-1-4939-6676-9.
66. J.D. Bass, *Mineral Physics & Crystallography*, American Geophysical Union (AGU), Washington, 1995, pp. 45–63. https://doi.org/10.1029/RF002p0045.
67. S. Mobasher Moghaddam, F. Sadeghi, K. Paulson, N. Weinzapfel, M. Correns, V. Bakolas, and M. Dinkel: *Int. J. Fatigue*, 2015, vol. 80, pp. 203–15. https://doi.org/10.1016/j.ijfatigue.2015.05.010.
68. R. Prasannavenkatesan, D.L. McDowell, G.B. Olson, and H.-J. Jou: *J. Eng. Mater. Technol.*, 2008. https://doi.org/10.1115/1.3030943.
69. D.G. Isaak, O.L. Anderson, T. Goto, and I. Suzuki: *J. Geophys. Res. Solid Earth*, 1989, vol. 94, pp. 5895–5906. https://doi.org/10.1029/JB094iB05p05895.